



D5

Paper on the developed hyperspectral multispecies calibration method

Paper in the fulfilment of A2.3.6

Authors

Guillermo Andrés Guarnizo Herreño and Juan Meléndez (UC3M)

Dolores Del Campo (CEM)

Stefan Persijn (VSL)

EMPIR Grant Agreement number: 16ENV08

Project short name: IMPRESS 2

Organisation name of lead partner for the deliverable: VSL B.V.

Due date of the deliverable: 31 May 2019

Actual submission date of the deliverable: 15 February 2021



Contents

1	Traceable calibration methods for hyperspectral imagers at U3CM.....	3
1.1	Infrared spectroscopy for gas quantification.....	3
1.2	Radiometric model.....	4
1.3	Estimation of uncertainty in column density: absorption mode	5
1.3.1	Systematic error in absorption spectroscopy due to gas emission	5
1.3.2	Uncertainty in absorption spectroscopy due to measurement noise	6
1.4	Estimation of uncertainty in column density: emission mode	8
1.4.1	Uncertainty due to calibration.....	9
2	Comparison of the hyperspectral calibration procedures on gas reference mixtures at U3CM..	11
3	OPO development and HCl measurements at VSL	18



1 Traceable calibration methods for hyperspectral imagers at U3CM

1.1 Infrared spectroscopy for gas quantification

The detection and quantification of gases by infrared (IR) spectroscopy is based on their emission/absorption properties. All gaseous molecules with a dipolar momentum have rotational energy levels, and the quantum transitions between them have energies in the infrared range. Since these levels depend on the masses of the atoms and the geometry of the molecules, they are highly specific, and thus each chemical species can be identified by its characteristic absorption or emission spectrum (commonly called “IR fingerprint”). Quantification is also possible, since not only the wavenumbers but also the absorptivities of these transitions, and its dependence on temperature, are well known and can be found on spectroscopic databases like PNNL Quantitative IR [1] or HITRAN [2].

For a specific line at wavenumber ν with absorptivity a , gas transmittance is given by the well-known Lambert-Beer law:

$$\tau_g(\nu, C_g, T_g) = e^{-a(\nu, T_g)C_g L_g} \equiv e^{-a(\nu, T_g)Q_g} \quad (1)$$

where L_g is the gas optical path, C_g is the gas concentration, $Q_g = C_g L_g$ is the column density (usually measured in ppm·m), and the dependence of a on wavenumber and temperature has been shown explicitly. If there are more than one absorbing species, $\tau(\nu)$ is just a product of terms like this, one for each species; if the concentration is not homogeneous, the product aCL is replaced by an integral.

This is the basis of IR absorption spectroscopy, a classical method of analytical chemistry. In a typical laboratory implementation, a gas cell within a spectrophotometer is filled with the sample to be measured, and then with a reference gas (typically N_2) without absorption lines in the spectral region of interest. Transmittance is obtained as the ratio of the two spectra, and assuming $a(\nu, T_g)$ and L_g are known, the Lambert-Beer law (1) is solved for C_g .

On the other hand, since Kirchhoff's law states that under the condition of local thermodynamic equilibrium the absorptance α equals the emittance, $\alpha = \varepsilon$, it turns out that for a gas $\varepsilon + \tau = 1$ and thus $\varepsilon = 1 - \tau$. Therefore, the transmittance spectrum provides the same information as the emissivity spectrum, and emission spectra can also be used to identify and quantify gas species.

In field measurements, both emission and absorption effects may be important and must be accounted for by a radiometric model. Also, usually there will not be a well-defined length L_g , and the aim will be to determine the value of column density Q_g . The radiometric model should make it possible to evaluate the uncertainty of column density measurements both in absorption spectroscopy (transmittance measurements) or emission spectroscopy (radiance measurements) and therefore suggests the best measurement strategy as a function of gas parameters (temperature, expected concentration, spectral band of the absorption/emission features, etc), as well as establishing the requirements for radiometric calibration of the radiometer.

¹ Sharpe, S. W., Sams, R. L., & Johnson, T. J. (2002). The PNNL quantitative IR database for infrared remote sensing and hyperspectral imaging. Paper presented at the Proceedings - Applied Imagery Pattern Recognition Workshop; 31st Applied Imagery Pattern Recognition Workshop, AIPR 2002, 2002-January 45-48. doi:10.1109/AIPR.2002.1182253

² Gordon, I. E., Rothman, L. S., Hill, C., Kochanov, R. V., Tan, Y., Bernath, P. F., . . . Zak, E. J. (2017). The HITRAN2016 molecular spectroscopic database. doi:https://doi.org/10.1016/j.jqsrt.2017.06.038

1.2 Radiometric model

Figure 1 shows the schematic diagram of a generic measurement configuration. The following simplifying assumptions will be made:

1. The gas is in local thermal equilibrium, so that Boltzmann distribution holds and absorptance (a) equals emittance (ε) (Kirchhoff's Law). The effects of absorption and scattering by particulate matter are negligible.
2. For each pixel, the gas is modelled by a single temperature and a single value of concentration for each species (these values are considered as line-of-sight averages); therefore the gas cloud can be characterized by a single transmittance τ_g and emissivity $\varepsilon_g = 1 - \tau_g$ at each pixel.
3. The background emissivity ε_b is large, so that the reflection of ambient radiation in the background is negligible.
4. The emission of the atmosphere is negligible (i.e., near transparent spectral region, and/or ambient temperature T_a much lower than those of gas cloud and background).

With these approximations, the radiance measured by the radiometer is:

$$\mathcal{L}^{in} = \mathcal{L}_m = \mathcal{L}^B(T_b) \cdot \varepsilon_b \cdot \tau_{a_1} \tau_g \tau_{a_2} + \mathcal{L}^B(T_g) \cdot (1 - \tau_g) \tau_{a_2} \quad (2)$$

where τ_g , τ_{a_1} and τ_{a_2} are, respectively, the transmittances of the gas cloud and the first and second atmospheric paths

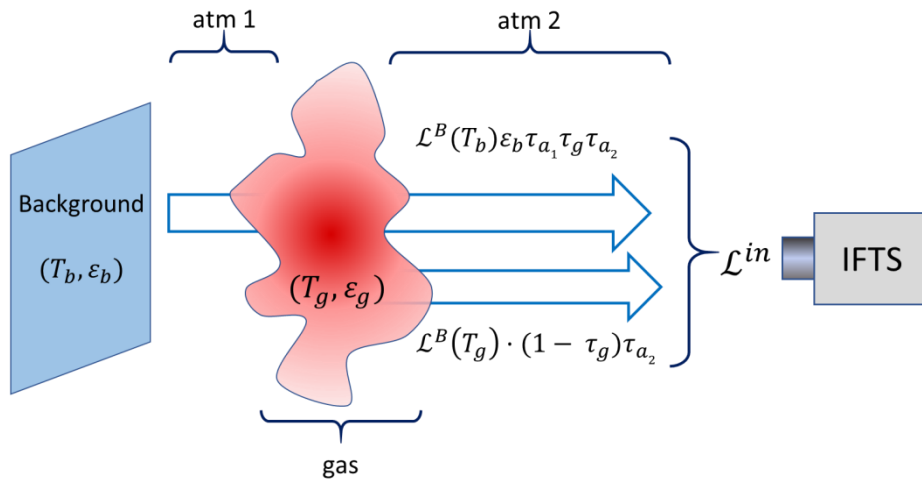


Figure 1), \mathcal{L}^B stands for Planck's blackbody radiance, and T_b , T_g are, respectively, the temperatures of background and gas cloud.

To obtain a transmittance measurement, a reference spectrum must be measured without absorbing gas:

$$\mathcal{L}^{in} = \mathcal{L}_r = \mathcal{L}^B(T_b) \cdot \varepsilon_b \cdot \tau_{a_1} \tau_{g_0} \tau_{a_2} \quad (3)$$

where τ_{g_0} stands for the transmittance of the path that was previously occupied by the gas cloud; it will be assumed that $\tau_{g_0} \approx 1$.

A nominal transmittance is obtained as the ratio:

$$\tau_{\text{nom}} \equiv \frac{\mathcal{L}_m}{\mathcal{L}_r} = \tau_g + \frac{\mathcal{L}^B(T_g)}{\mathcal{L}^B(T_b)} \cdot (1 - \tau_g) \cdot \frac{1}{\varepsilon_b \tau_{a_1}} \equiv \tau_g + \tau' \quad (4)$$

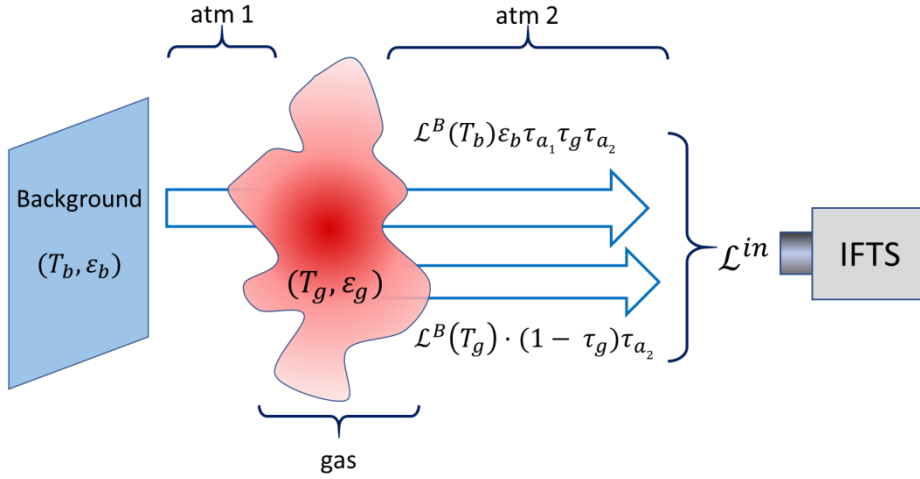


Figure 1. Schematics of the radiative model

The nominal transmittance (4) is the starting point of absorption spectroscopy. Alternatively, it is possible to dispense with the reference altogether and use only the emission spectrum: that is the case of emission spectroscopy. In both cases, the most powerful approach is to compare the experimental spectra (of transmittance or radiance) with simulated spectra over a certain spectral range, and to retrieve the values of column density of the gas, and possibly also temperature, as those values that provide a best fit. This has been done in references [3] and [4].

However, in order to gain insight on the main factors involved, it is useful to perform a simple estimation of the uncertainty in the retrieved Q_g values. This will be done in the next sections, where for simplicity it will be assumed that (a) a single wavenumber of known absorptivity is used and (b) the gas temperature is known. We will start with absorption spectroscopy.

1.3 Estimation of uncertainty in column density: absorption mode

1.3.1 Systematic error in absorption spectroscopy due to gas emission

Nominal transmittance (eq. 4) differs from the real gas transmittance by the positive term τ' . Using τ_{nom} instead of τ_g will result in a systematic error, whose magnitude can be estimated as follows. Assuming $\tau_{a_1} \approx 1$, writing $\varepsilon_{\text{nom}} = 1 - \tau_{\text{nom}}$ and $\varepsilon_g = 1 - \tau_g$ and, for simplicity, $\mathcal{L}_g \equiv \mathcal{L}^B(T_g)$ (blackbody radiance at the gas temperature) and $\mathcal{L}_b \equiv \mathcal{L}^B(T_b) \cdot \varepsilon_b$ (radiance emitted by the background), ε_{nom} can be written, according to eq. (4), as

$$\varepsilon_{\text{nom}} \approx \varepsilon_g \left(1 - \frac{\mathcal{L}_g}{\mathcal{L}_b} \right) \equiv \varepsilon_g \cdot f \quad (5)$$

where f is a function of ε_b , T_b and T_g . Thus,

³ Rodríguez-Conejo, M. A., & Meléndez, J. (2015). Hyperspectral quantitative imaging of gas sources in the mid-infrared. *Applied Optics*, 54(2), 141-149. doi:10.1364/AO.54.000141

⁴ Sutton, G., Fateev, A., Rodríguez-Conejo, M. A., Meléndez, J., & Guarnizo, G. (2019). Validation of emission spectroscopy gas temperature measurements using a standard flame traceable to the international temperature scale of 1990 (ITS-90). *International Journal of Thermophysics*, 40(11) doi:10.1007/s10765-019-2557-6



$$\frac{\varepsilon_{\text{nom}} - \varepsilon_g}{\varepsilon_g} = \frac{\Delta\varepsilon}{\varepsilon} \approx -\frac{\mathcal{L}_g}{\mathcal{L}_b} \quad (6)$$

Expanding Lambert-Beer law to first order, $\varepsilon = 1 - \tau = 1 - e^{-\alpha Q} \approx \alpha Q$. Therefore, for small values of Q , using ε_{nom} instead of ε_g causes a systematic error

$$\left(\frac{\Delta Q}{Q}\right)_{\varepsilon_{\text{nom}}} \approx \frac{\Delta\varepsilon}{\varepsilon} \approx -\frac{\mathcal{L}_g}{\mathcal{L}_b} \quad (7)$$

This error is always negative, i.e., the retrieved Q is smaller than the real value because the emission contribution is not taken into account (in the extreme case $T_b = T_g$, $(\Delta Q/Q)_{\varepsilon_{\text{nom}}} = -100\%$ meaning that retrieved Q is 0 ppm·m, as expected since in that case there is no thermal contrast and $\tau_{\text{nom}} = 1$). The smaller the thermal contrast between gas and background, the worse approximation will be to take τ_{nom} as the gas transmittance.

As an example, for an absorption line at $\mu = 3.3 \mu\text{m}$ (typical for hydrocarbons) with $T_g = 25^\circ\text{C}$, the relative error will be only $(\Delta Q/Q)_{\varepsilon_{\text{nom}}} \approx -0.05\%$ if the background is a blackbody at $T_b = 350^\circ\text{C}$, whereas for $T_b = 50^\circ\text{C}$, $(\Delta Q/Q)_{\varepsilon_{\text{nom}}} \approx -32.5\%$.

It is clear therefore that, although the errors involved are small as long as the condition $T_g \ll T_b$ holds, the effect of gas emission should be taken into account in order to expand the applicability of absorption spectroscopy as much as possible. This amounts simply to use the correction factor $f \equiv \left(1 - \frac{\mathcal{L}_g}{\mathcal{L}_b}\right)$ to estimate ε_g from ε_{nom} , i.e., $\varepsilon_g = \varepsilon_{\text{nom}}/f$.

This correction requires knowing the temperatures of background and gas. For the sake of uncertainty estimation it will be assumed that both are known. In real measurement situations, T_b is nearly always known, at least approximately; T_g may be unknown but can be retrieved by fitting experimental spectra with simulated ones, as mentioned before.

1.3.2 Uncertainty in absorption spectroscopy due to measurement noise

We proceed now to estimate the relative uncertainty in Q for absorption mode measurements when the corrected value for ε_g is used. An appealing feature of transmittance spectroscopy is that, since τ is obtained as a ratio of measurements, it is not necessary that spectra are calibrated in radiometric units, but only that the system response is linear. However, uncertainty due to measurement noise may be important in some situations, and its magnitude must be assessed.

Since $\varepsilon_{\text{nom}} = 1 - \tau_{\text{nom}} = 1 - \mathcal{L}_m/\mathcal{L}_r$ and, to first order, $\varepsilon \approx \alpha Q$ (small value of Q), eq. (5) becomes

$$\varepsilon_g \approx \alpha Q \approx \frac{1 - \mathcal{L}_m/\mathcal{L}_r}{1 - \mathcal{L}_g/\mathcal{L}_b} \quad (8)$$

and therefore

$$\frac{d\varepsilon_g}{\varepsilon_g} \approx \frac{dQ}{Q} = \frac{-d\mathcal{L}_m \cdot \mathcal{L}_r + d\mathcal{L}_r \cdot \mathcal{L}_m}{\mathcal{L}_r(\mathcal{L}_r - \mathcal{L}_m)} - \frac{-d\mathcal{L}_g \cdot \mathcal{L}_b + d\mathcal{L}_b \cdot \mathcal{L}_g}{\mathcal{L}_b(\mathcal{L}_b - \mathcal{L}_g)} \quad (9)$$

It will be assumed here that $\tau_{a_1} \approx \tau_{a_2} \approx 1$. Then, $\mathcal{L}_r - \mathcal{L}_m = (1 - \tau_g) \cdot (\mathcal{L}_b - \mathcal{L}_g)$. Writing uncertainties as increments instead of differentials and adding them up in quadrature,



$$\begin{aligned} \left(\frac{\Delta Q}{Q}\right)_{abs}^2 &\approx \frac{1}{(\mathcal{L}_b - \mathcal{L}_g)^2} \left\{ \left(\frac{\Delta \mathcal{L}_m}{1 - \tau_g}\right)^2 + \left(\frac{\Delta \mathcal{L}_r}{1 - \tau_g}\right)^2 \frac{\mathcal{L}_m^2}{\mathcal{L}_r^2} + (\Delta \mathcal{L}_g)^2 + (\Delta \mathcal{L}_b)^2 \cdot \frac{\mathcal{L}_g^2}{\mathcal{L}_b^2} \right\} \equiv \\ &\equiv \left(\frac{\Delta Q}{Q}\right)_m^2 + \left(\frac{\Delta Q}{Q}\right)_r^2 + \left(\frac{\Delta Q}{Q}\right)_g^2 + \left(\frac{\Delta Q}{Q}\right)_b^2 \end{aligned} \quad (10)$$

The relative uncertainty of Q measured in absorption mode is written thus as the sum of four terms, all of them inversely proportional to the thermal contrast ($\mathcal{L}_b - \mathcal{L}_g$). The first two are also inversely proportional to the radiometric signal (the effect on transmittance of the gas cloud, $1 - \tau_g$), and account for the effect of uncertainties in the measured radiances ($\Delta \mathcal{L}_m$, $\Delta \mathcal{L}_r$), due to noise or calibration errors. We will write $\left(\frac{\Delta Q}{Q}\right)_m^2 + \left(\frac{\Delta Q}{Q}\right)_r^2 \equiv \left(\frac{\Delta Q}{Q}\right)_L^2$

The third and fourth terms account for the effect of uncertainties in the temperatures of gas and background. We will write $\left(\frac{\Delta Q}{Q}\right)_g^2 + \left(\frac{\Delta Q}{Q}\right)_b^2 \equiv \left(\frac{\Delta Q}{Q}\right)_T^2$. In fact, it is easy to see that $\left(\frac{\Delta Q}{Q}\right)_L = \frac{\Delta \epsilon_{nom}}{\epsilon_{nom}}$ and $\left(\frac{\Delta Q}{Q}\right)_T = \frac{\Delta f}{f}$ and therefore the second term represents the additional ΔQ due to uncertainty in the correction factor f .

In order to calculate $\left(\frac{\Delta Q}{Q}\right)_L$ it is necessary to know the values of $\Delta \mathcal{L}_r$ and $\Delta \mathcal{L}_m$. These are intrinsic parameters of the measurement instrument, so it can be written $\Delta \mathcal{L}_r \approx \Delta \mathcal{L}_m \equiv \Delta \mathcal{L}_{noise}$, and $\Delta \mathcal{L}_{noise}$ can be estimated from the experimental noise to signal ratio, $\epsilon_L \equiv \frac{\Delta \mathcal{L}_r}{\mathcal{L}_r}$. Measurements have been performed with a Telops Hypercam IFTS instrument⁵, for a gas cell filled with N_2 , with $T_b = 350^\circ C$, and it has been found that $\epsilon_L \sim 0.01$ for $\nu \approx 2900 \text{ cm}^{-1}$. Since $\mathcal{L}_r \approx \mathcal{L}_b$, a numerical value $\Delta \mathcal{L}_r$ is obtained as $\Delta \mathcal{L}_r \sim \epsilon_L \cdot \mathcal{L}^B(T_b) \sim 0.01 \cdot \mathcal{L}^B(350^\circ C) \approx 3.6 \text{ mW/m}^2 \cdot \text{sr} \cdot \text{cm}^{-1}$.

Another independent estimation for $\Delta \mathcal{L}_r$ is provided by the Noise Equivalent Spectral Radiance (NESR) of the instrument. This parameter is related to the Noise Equivalent Power (NEP) of the detector by [6]

$$NESR = \frac{NEP}{0.5 \cdot \tau \cdot EM \cdot \Theta \cdot \Delta \nu \cdot \sqrt{t}} \quad (11)$$

where τ is the transmittance of the system, EM the modulation efficiency, Θ the throughput, $\Delta \nu$ the spectral spacing and t the integration time. According to the specifications of the TELOPS instrument, the NESR in the spectral range of interest, measured with $t = 300 \mu s$ and $\Delta \nu = 16 \text{ cm}^{-1}$ is $\approx 5 \cdot 10^{-5} \text{ W/m}^2 \text{sr} \cdot \text{cm}^{-1}$. In our case, $t = 10 \mu s$ and $\Delta \nu = 1 \text{ cm}^{-1}$ and the rest of the parameters are the same, so that $NESR \approx 4.4 \text{ mW/m}^2 \text{sr} \cdot \text{cm}^{-1}$, in reasonable agreement with the experimental $\Delta \mathcal{L}_{noise}$ value $3.6 \text{ mW/m}^2 \cdot \text{sr} \cdot \text{cm}^{-1}$.

⁵ M. Chamberland, V. Farley, A. Vallières, A. Villemaire, L. Belhumeur, J. Giroux, and J.-F. Legault, "High-performance field-portable imaging radiometric spectrometer technology for hyperspectral imaging applications," Proc. SPIE 5994,59940N (2005).

⁶ Farley, V., Chamberland, M., Vallières, A., Villemaire, A., & Legault, J. -. (2006). Radiometric calibration stability of the FIRST: A longwave infrared hyperspectral imaging sensor. Paper presented at the *Proceedings of SPIE - the International Society for Optical Engineering*, 6206 // .doi:10.1117/12.665888

For the case of “cold” gas, $\mathcal{L}_g \ll \mathcal{L}_b$ and thus $\mathcal{L}_m/\mathcal{L}_r \approx \tau_g$, the approximation $\left(\frac{\Delta Q}{Q}\right)_L \approx \epsilon_L \frac{\sqrt{1+\tau_g^2}}{1-\tau_g}$ holds. As an example, for a room temperature gas with $\tau_g \approx 0.8$ at 2900 cm^{-1} and a blackbody at 350°C as background, using $\epsilon_L \sim 0.01$ gives $\left(\frac{\Delta Q}{Q}\right)_L \approx 6.4\%$.

On the other hand, $(\Delta Q/Q)_T$ can be easily calculated assuming the uncertainties of T_g and T_b . For a gas at room temperature with $T_b = 350^\circ\text{C}$, assuming $\Delta T_g = \Delta T_b = 1^\circ\text{C}$, it is found that $\left(\frac{\Delta Q}{Q}\right)_T \approx 0.003\%$, a negligible value as compared to $\left(\frac{\Delta Q}{Q}\right)_L$.

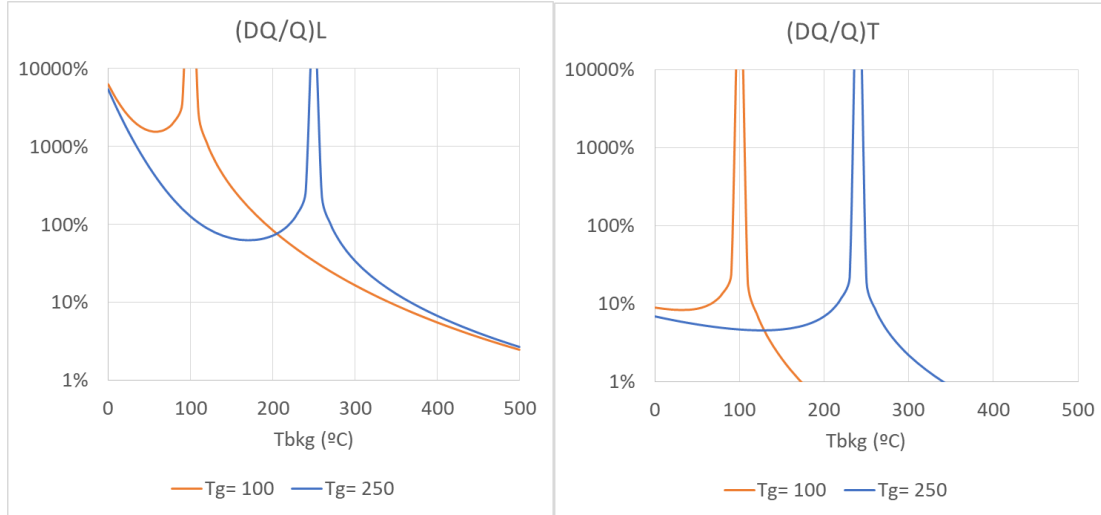


Figure 2. Relative uncertainties in column density Q . (Left): $\left(\frac{\Delta Q}{Q}\right)_L$, due to measurement noise. (Right): $\left(\frac{\Delta Q}{Q}\right)_T$, due to uncertainties in background and gas temperature, assumed to be both $\pm 1\text{K}$

Values of $\left(\frac{\Delta Q}{Q}\right)_L$ and $\left(\frac{\Delta Q}{Q}\right)_T$ are plotted in Figure 2 against background temperature T_b , for two different values of gas temperature T_g using the previous $\Delta \mathcal{L}_r$ value. It is apparent that, although emission correction enables to measure in absorption mode even when the condition $T_g \ll T_b$ does not hold, nevertheless errors become very large when a realistic noise level in the measurement is assumed. In particular, when the background is cooler than the gas the relative uncertainty of Q measurements in transmittance mode is always very large, exceeding a value of 60% for all cases.

In addition, it can be concluded that uncertainty in Q due to the correction factor, $\left(\frac{\Delta Q}{Q}\right)_T$, is always negligible as compared to uncertainty due measured radiances, $\left(\frac{\Delta Q}{Q}\right)_L$, for reasonable values of $\Delta T_g, \Delta T_b$.

1.4 Estimation of uncertainty in column density: emission mode

The starting point for emission spectroscopy is equation (2). Assuming $\tau_{a_1} \approx \tau_{a_2} \approx 1$ and writing, as before, $\mathcal{L}_g \equiv \mathcal{L}^B(T_g)$ and $\mathcal{L}_b \equiv \mathcal{L}^B(T_b) \cdot \epsilon_b$, this equation can be written as

$$\mathcal{L}_m \approx \mathcal{L}_b \cdot \tau_g + \mathcal{L}_g \cdot (1 - \tau_g) \quad (1210)$$



Since $\varepsilon_g = 1 - \tau_g$ and for low gas concentration $\varepsilon_g \approx \alpha Q$, $\mathcal{L}_m \approx \mathcal{L}_b \cdot (1 - \alpha Q) + \mathcal{L}_g \cdot \alpha Q$, and solving for αQ :

$$\alpha Q \approx \frac{1 - \mathcal{L}_m / \mathcal{L}_b}{1 - \mathcal{L}_g / \mathcal{L}_b} \quad (13)$$

This equation is completely analogous to (8) except that \mathcal{L}_r has been replaced by \mathcal{L}_b . Therefore, the relative uncertainty in Q measured in emission is given by an expression analogous to (9), with \mathcal{L}_b instead of \mathcal{L}_r

$$\frac{d\varepsilon_g}{\varepsilon_g} \approx \frac{dQ}{Q} = \frac{-d\mathcal{L}_m \cdot \mathcal{L}_b + d\mathcal{L}_b \cdot \mathcal{L}_m}{\mathcal{L}_b(\mathcal{L}_b - \mathcal{L}_m)} - \frac{-d\mathcal{L}_g \cdot \mathcal{L}_b + d\mathcal{L}_b \cdot \mathcal{L}_g}{\mathcal{L}_b(\mathcal{L}_b - \mathcal{L}_g)} \quad (14)$$

Now this can be simplified as

$$\frac{dQ}{Q} = \frac{-d\mathcal{L}_m}{\mathcal{L}_b - \mathcal{L}_m} + \frac{d\mathcal{L}_g}{\mathcal{L}_b - \mathcal{L}_g} - \frac{d\mathcal{L}_b}{\mathcal{L}_b - \mathcal{L}_g} \cdot \frac{\mathcal{L}_g - \mathcal{L}_m}{\mathcal{L}_b - \mathcal{L}_m}$$

And thus, since $\mathcal{L}_b - \mathcal{L}_m = (1 - \tau_g) \cdot (\mathcal{L}_b - \mathcal{L}_g)$,

$$\begin{aligned} \left(\frac{\Delta Q}{Q}\right)_{emis}^2 &\approx \frac{1}{(\mathcal{L}_b - \mathcal{L}_g)^2} \left\{ \left(\frac{\Delta \mathcal{L}_m}{1 - \tau_g}\right)^2 + (\Delta \mathcal{L}_g)^2 + (\Delta \mathcal{L}_b)^2 \cdot \frac{(\mathcal{L}_g - \mathcal{L}_m)^2}{(\mathcal{L}_b - \mathcal{L}_m)^2} \right\} \equiv \\ &\equiv \left(\frac{\Delta Q}{Q}\right)_m^2 + \left(\frac{\Delta Q}{Q}\right)_g^2 + \left(\frac{\Delta Q}{Q}\right)_b^2 \end{aligned} \quad (15)$$

Comparison of this equation to the uncertainty in transmittance given by eq. (10) shows that the term $\left(\frac{\Delta Q}{Q}\right)_r$ has disappeared, and in the term $\left(\frac{\Delta Q}{Q}\right)_b$ there is a factor $\frac{|\mathcal{L}_g - \mathcal{L}_m|}{|\mathcal{L}_b - \mathcal{L}_m|}$ instead of $\frac{\mathcal{L}_g}{\mathcal{L}_b}$, which makes it smaller. These two differences decrease the uncertainty, but, on the other hand, uncertainties in radiance due to calibration must now be included in $\Delta \mathcal{L}_m$ in addition to uncertainty due to noise.

1.4.1 Uncertainty due to calibration

The process of calibration of an IFTS assumes a linear response, so that the experimental spectrum is

$$S^{exp}(\nu) = G(\nu) \cdot (\mathcal{L}_{ext}(\nu) + \mathcal{L}_{off}(\nu)) \quad (16)$$

Where $\mathcal{L}_{ext}(\nu)$ is the external radiance that reaches the system and $\mathcal{L}_{off}(\nu)$ is the parasitic radiance emitted by the internal parts that contributes an offset term. To determine the spectral gain $G(\nu)$, measurements of a blackbody radiator are performed at short distances, in order that atmospheric effects are negligible. Two spectra are measured for two different blackbody temperatures, "hot" (T_2) and "cold" (T_1) that span the range of temperatures expected:

$$S_1 = G \cdot (\mathcal{L}_{ext1} + \mathcal{L}_{off})$$

$$S_2 = G \cdot (\mathcal{L}_{ext2} + \mathcal{L}_{off})$$

Solving for G , it is found that

$$G = \frac{S_2 - S_1}{\mathcal{L}_{ext2} - \mathcal{L}_{ext1}} \quad (17)$$

To obtain a calibrated radiance spectrum, an offset spectrum S_0 is acquired first, by filling the field of view of the instrument with a cold plate (at $\approx -20^\circ\text{C}$). Then, this is subtracted from the measured spectrum S^m , and the result is converted to radiance units dividing by the gain G :

$$\mathcal{L}_{\text{cal}} = \frac{S_m - S_0}{G} = \frac{S_m - S_0}{S_2 - S_1} (\varepsilon_{\text{BB}} \mathcal{L}_{\text{BB}}(T_2) - \varepsilon_{\text{BB}} \mathcal{L}_{\text{BB}}(T_1)) \quad (18)$$

where it has been written $\mathcal{L}_{\text{ext}1} = \varepsilon_{\text{BB}} \mathcal{L}_{\text{BB}}(T_1)$, $\mathcal{L}_{\text{ext}2} = \varepsilon_{\text{BB}} \mathcal{L}_{\text{BB}}(T_2)$, assuming an emissivity ε for the blackbody to account for non idealities. The measured radiance spectrum can be written as the product of two factors, $\mathcal{L}_{\text{cal}} = A \cdot B$ where $A \equiv \frac{S_m - S_0}{S_2 - S_1}$ contains the experimental spectral measurements and $B \equiv \varepsilon \mathcal{L}_{\text{CN}}(T_2) - \varepsilon \mathcal{L}_{\text{CN}}(T_1)$ the nominal values of radiance used for the calibration. Then, $\frac{d\mathcal{L}_{\text{cal}}}{\mathcal{L}_{\text{cal}}} = \frac{dA}{A} + \frac{dB}{B}$.

The first term can be estimated as follows:

$$\frac{dA}{A} = \frac{dS_m - dS_0}{S_m - S_0} - \frac{dS_2 - dS_1}{S_2 - S_1} = \frac{d\mathcal{L}_m - d\mathcal{L}_0}{\mathcal{L}_m - \mathcal{L}_0} - \frac{d\mathcal{L}_{\text{ext}2} - d\mathcal{L}_{\text{ext}1}}{\mathcal{L}_{\text{ext}2} - \mathcal{L}_{\text{ext}1}} \quad (19)$$

And the second

$$\frac{dB}{B} = \frac{d\varepsilon_{\text{BB}}}{\varepsilon_{\text{BB}}} + \frac{d\mathcal{L}_{\text{ext}2} - d\mathcal{L}_{\text{ext}1}}{\mathcal{L}_{\text{ext}2} - \mathcal{L}_{\text{ext}1}} \quad (20)$$

Hence

$$\frac{d\mathcal{L}_{\text{cal}}}{\mathcal{L}_{\text{cal}}} = \frac{d\mathcal{L}_m - d\mathcal{L}_0}{\mathcal{L}_m - \mathcal{L}_0} + \frac{d\varepsilon_{\text{BB}}}{\varepsilon_{\text{BB}}}$$

And therefore

$$\left(\frac{\Delta\mathcal{L}_{\text{cal}}}{\mathcal{L}_{\text{cal}}}\right)^2 = \frac{(\Delta\mathcal{L}_m)^2 + (\Delta\mathcal{L}_0)^2}{(\mathcal{L}_m - \mathcal{L}_0)^2} + \left(\frac{\Delta\varepsilon_{\text{BB}}}{\varepsilon_{\text{BB}}}\right)^2 \approx 2 \left(\frac{\Delta\mathcal{L}_{\text{noise}}}{\mathcal{L}_m}\right)^2 + \left(\frac{\Delta\varepsilon_{\text{BB}}}{\varepsilon_{\text{BB}}}\right)^2 \quad (21)$$

Where it has been assumed that $\Delta\mathcal{L}_m \approx \Delta\mathcal{L}_0 \approx \Delta\mathcal{L}_{\text{noise}}$ and $\mathcal{L}_0 \ll \mathcal{L}_m$.

According to the specifications of the blackbody used for calibration, $\varepsilon_{\text{BB}} = 0.9841$ and $\Delta\varepsilon_{\text{BB}} = 0.02$, so that $\frac{\Delta\varepsilon_{\text{BB}}}{\varepsilon_{\text{BB}}} \sim 2\%$. Using, as previously, $\Delta\mathcal{L}_{\text{noise}} = 3.6 \text{ mW/m}^2 \cdot \text{sr} \cdot \text{cm}^{-1}$, $\tau_g \approx 0.8$ for an emission line at 2900 cm^{-1} and a background at room temperature, the term $2 \frac{\Delta\mathcal{L}_{\text{noise}}}{\mathcal{L}_m}$ is $\sim 10\%$ for $T_g = 350^\circ\text{C}$, and $\sim 0.7\%$ for $T_g = 750^\circ\text{C}$.

The value of $\Delta\mathcal{L}_{\text{cal}}$ obtained from equation (21) is the one to be used instead of $\Delta\mathcal{L}_m$ in the expression of uncertainty in emission (15) in order to take into account the effect of calibration. For the values just mentioned of τ_g, ν and T_b , $\left(\frac{\Delta Q}{Q}\right)_{\text{emis}} \approx 12\%$ for $T_g = 350^\circ\text{C}$, and $\sim 2.8\%$ for $T_g = 750^\circ\text{C}$.

2 Comparison of the hyperspectral calibration procedures on gas reference mixtures at U3CM

Introduction

In this part of the document the obtained laboratory results from the absorption measurements of the gas mixtures methane (CH₄), nitrous oxide (N₂O) and propane (C₃H₈) prepared by CEM (Spanish Metrology Institute) are presented. Apart from the identification and quantification tasks, some intermediate processing steps are presented and explained in order to justify the robustness of the hyperspectral method in air pollutant quantification.

The concentration values of the gas mixtures were agreed among the three partners taking into account the environment measurement conditions at LIR-UC3M and VSL as well as the ease of substance availability at CEM. These concentration values are displayed in Table 1 just as the column density values (for a 43-cm gas cell used at LIR-UC3M) of particular interest for the hyperspectral method.

Pollutant gas	Concentration (ppm)	Column density (ppm·m)
Methane (CH ₄)	600	258
Nitrous oxide (N ₂ O)	250	107.5
Propane (C ₃ H ₈)	500	215

Table 1. Air pollutant concentrations

Experimental Setup

It is intended to measure the pollutant concentration inside a metallic gas cell based on its spectral transmittance. With this aim, two measurements are going to be performed: The first one comprises the gas cell filled with target pollutant and the second one the same gas cell filled with a MIR (mid-infrared) transparent gas (namely, N₂). This experimental setup is displayed in Figure 2.

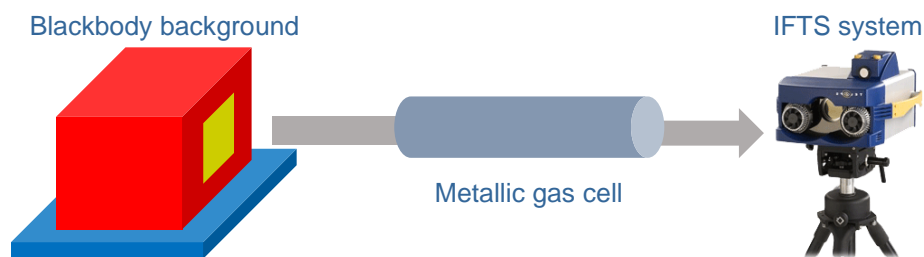


Figure 2. Setup for absorption-mode gas measurements

The radiation that incomes the Imaging Fourier Transform Spectrometer (IFTS) system with the gas cell filled with target pollutant can be considered to consist of two different terms: One coming from the background radiation that goes through the cell and the other coming from the gas inside the cell. The radiation of these areas are expressed in the next formula:

$$\mathcal{L}_{gas} = \mathcal{L}_{CN}(T_{back})\varepsilon_{back}\tau_{win 1}\tau_{amb 1}\tau_{win 2}\tau_{amb 2}\tau_{gas} + \mathcal{L}_{CN}(T_{gas})\varepsilon_{gas}\tau_{win 2}\tau_{amb 2}$$

where

\mathcal{L}_{CN} is the blackbody radiance at a defined temperature.

ε_{back} y ε_{gas} are the background and gas emissivities respectively.

T_{back} y T_{gas} are the background and gas temperatures respectively.

τ_{amb} , τ_{win} y τ_{gas} are the transmittances of ambient, cell windows and gas respectively. The subscripts 1 and 2 indicate the region between the background and the gas cell (1) and between the gas cell and the IFTS system (2).

Furthermore, the radiation that incomes the IFTS system coming from the reference measurement (\mathcal{L}_{ref}) is expressed in the next formula under the assumption that the N_2 transmittance inside the cell can be rounded to unity.

$$\mathcal{L}_{ref} = \mathcal{L}_{CN}(T_{back})\varepsilon_{back}\tau_{win\ 1}\tau_{amb\ 1}\tau_{win\ 2}\tau_{amb\ 2}$$

With the proposed setup and setting up a conventional bandwidth for hydrocarbons (2700 to 3200 cm^{-1}) the background integrated radiance (an extended blackbody radiator at 350°C which radiance would be around 150 $W/m^2cm^{-1}sr^{-1}$) is much higher than the one emitted by the pollutant cloud of e.g. methane at ambient temperature (which radiance would be around 0.05 $W/m^2cm^{-1}sr$), so the detected radiation at the presence of target gas is reduced to the first term:

$$\mathcal{L}_{gas}^{abs} \approx \mathcal{L}_{CN}(T_{back})\varepsilon_{back}\tau_{win\ 1}\tau_{amb\ 1}\tau_{win\ 2}\tau_{amb\ 2}\tau_{gas}$$

This allows us to calculate the value of transmittance linked to the pollutant gas as the ratio of the target gas radiance over the reference gas radiance without the need of radiometric calibration measurements and removing several error sources. With the previous considerations in mind, the next expression can be obtained:

$$\tau_{gas} \approx \frac{\mathcal{L}_{gas}^{abs}}{\mathcal{L}_{ref}}$$

The laboratory measurements were carried out for all the gas mixtures indicated previously (see Introduction) and a reference gas (N_2 at 100%). In all cases, the acquired spectra were recorded with its corresponding cold offsets references.

Measurement procedure

The next steps are required in order to obtain high-quality hyperspectral measurements with the setup displayed in Figure 2:

- 1) To check out that as the blackbody radiator as the IFTS system are properly configured:
 - Blackbody radiator surface temperature: 350°C.
 - IFTS system: Spectral resolution 1 cm^{-1} , region of interest (ROI) 256 x 160 pixels and integration time (T_{int}) 10 μs .
- 2) To verify the proper distances between the blackbody radiator and the gas cell (30 cm approx) and between the IFTS system and the gas cell (1.5 m approx). To frame the image displayed by the IFTS system (through its *FT Pro* software) that covers the total transversal gas cell area.
- 3) To fill the gas cell with the reference gas chosen (N_2) by opening both valves and letting the gas fluxes from the certified bottle during 15 seconds to guarantee it is completely filled. Next, the two valves are sealed for the measurements: First, an offset measurement with a cold slab in front of the IFTS system and then a measurement of the cell with the reference gas.
- 4) To repeat the previous step with the target air pollutant to be characterized.
- 5) To carry out the appropriate spectral processing to get the required identification and quantification information of the air pollutant.

Obtained results

Spatial window adjustment and spectral noise reduction

The first part of this post-measurement processing stage consists of zooming in on the part of the image strictly concerning the gas cell area to save time in the subsequent physical variables retrieval. As an example, the Figure 3 can be appreciated where an original image size of 256 x 160 pixels is reduced to 65 x 63 pixels before the subsequent spectral processing.

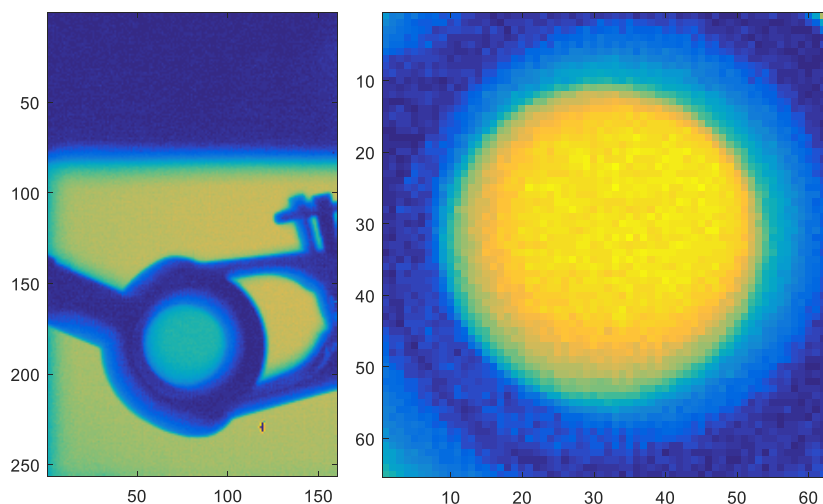


Figure 3. Spatial window adjustment. Left: Original image size. Right: Zoomed cell image.

The second part addresses the spectral noise reduction of experimental spectra through two steps: First, a non-supervised image classification procedure is carried out to establish the gas area inside the image (e.g. the central circle disk of the right image of Figure 3). Next, the spectra of this bounded region are processed according to a previously defined high percentage of explained variance to get the necessary principal components (PC). The original spectra are projected with this PCs and much less noisy spectra are obtained keeping the distinguishable spectroscopic signature of each air pollutant tested. This process may be regarded visually for the three examples displayed in Figure 4 for a central pixel in each of the gas mixtures analysed (methane (CH_4), nitrous oxide (N_2O) and propane (C_3H_8)).

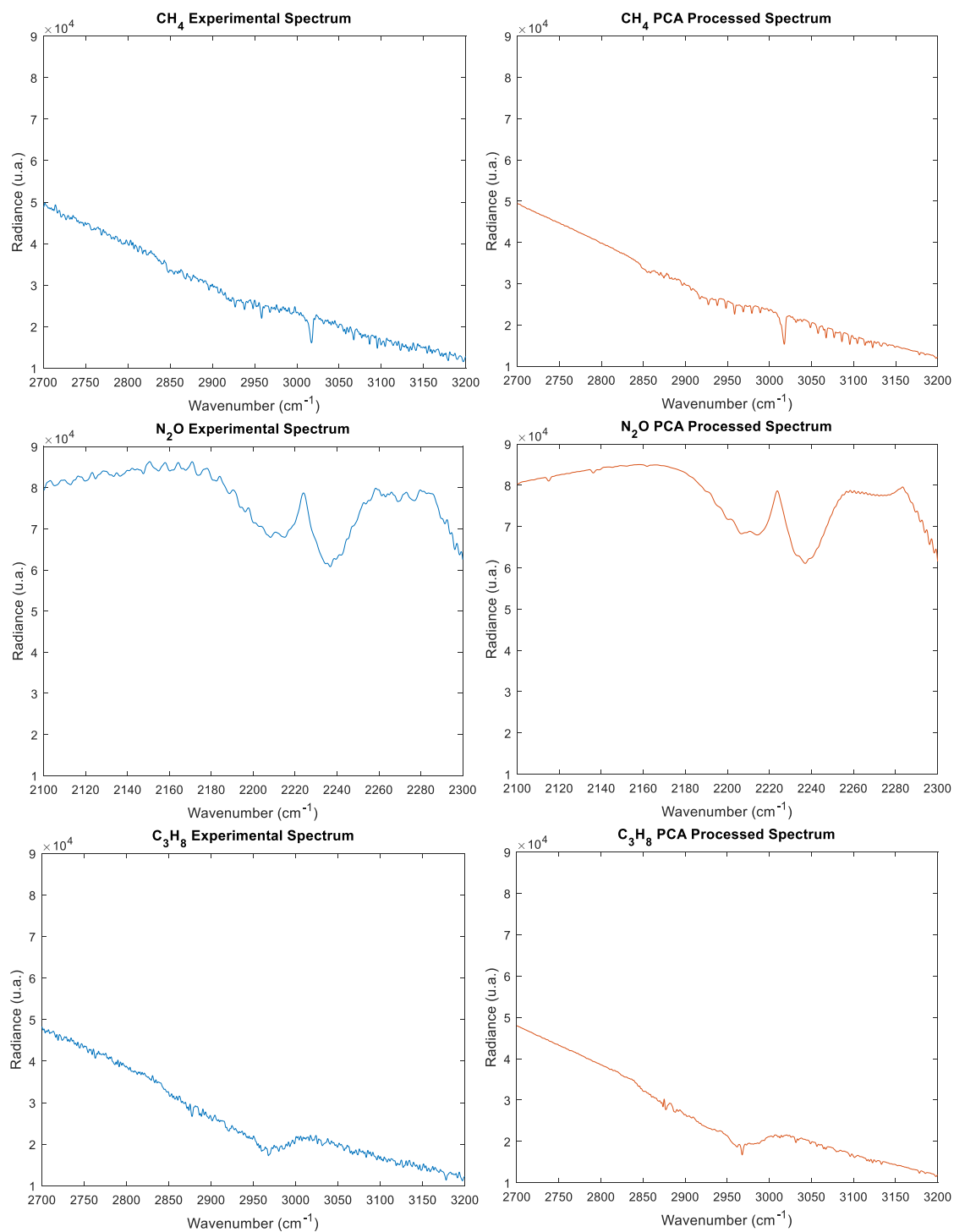


Figure 4. Spectral noise reduction. Left: Original experimental spectrum from a centred pixel for each air pollutant. Right: PCA noise reduced spectrum

Furthermore, the percentages of variance as well as the number of PCs obtained for each air pollutant are presented in Table 2.

Pollutant gas	% Variance	# PC
Methane (CH_4)	97	2
Nitrous oxide (N_2O)	99	2
Propane (C_3H_8)	97	4

Table 2. Variance percentage and Principal Components (PC) number for spectral noise reduction

Principal component analysis (PCA) spectral fitting comparisons

One remarkable effect of the previous noise spectral reduction is the enhancement in fitting between experimental and simulated transmittance looking for a precise recovery of the column density value directly related to the pollutant concentration. However, a dilemma about the noise reduction application is raised: Is it better to apply PCA noise reduction to radiance spectra to both, target gas and reference gas, before obtaining the transmittance through the ratio (case 1) or the opposite option, i.e. to make the ratio of radiances followed by applying PCA noise reduction to the transmittance (case 2)? In order to solve this question, an example with methane (CH_4) showing both cases of noise reduction are displayed in Figure 5. The value of the signal-to-noise ratio (SNR) in decibels for each case is also presented inside text boxes.

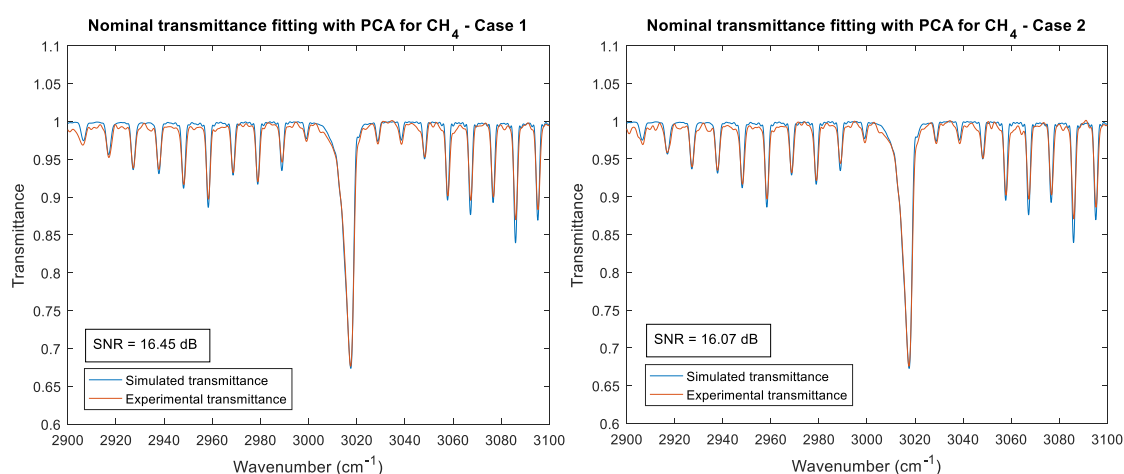


Figure 5. Graphical comparison of PCA noise reduction application in CH_4 . Left: Case 1. Right: Case 2

From the values presented in Figure 5 case 1 provide a slightly better noise reduction with PCA. This procedure also contributes to retrieve concentration values nearer the expected values. Figure 6 shows transmittance fitting comparisons for the three air pollutants tested in the project with measurements on the gas mixtures prepared by CEM, where the benefits of PCA implementation are clear.

Another way to show the benefits of PCA spectral noise reduction is through the SNR calculated value for each case. To obtain this ratio, we have defined as *signal* the simulated transmittance resulting from the fitting algorithm and as *noise* the deviation between experimental and simulated transmittance. The SNR results on a central gas cell pixel for the three air pollutants displayed in Figure 6 are presented in Table 3 where a notable improvement on these values is evident.

Pollutant gas	SNR without PCA (dB)	SNR with PCA (dB)
Methane (CH_4)	6.64	16.45
Nitrous oxide (N_2O)	24.35	26.30
Propane (C_3H_8)	13.34	25.81

Table 3. SNR value for a central pixel point without and with PCA noise reduction

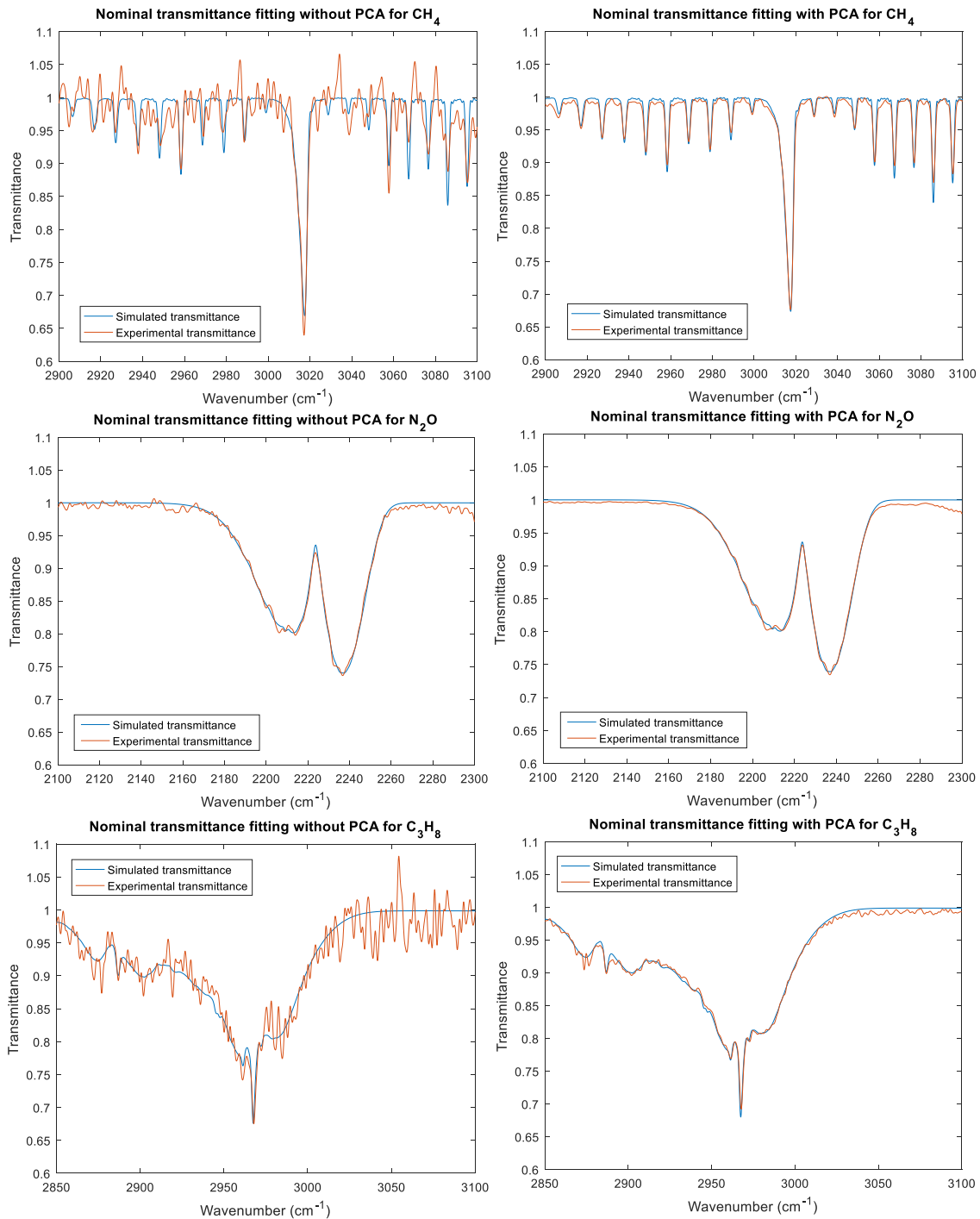


Figure 6. Transmittance fitting comparison without (left) and with (right) PCA noise reduction for the three air pollutants analysed

Air pollutants concentration maps

According to the experimental measurements compromised in task 2.3 of the IMPRESS 2 project, a series of retrieved density column maps of air pollutants are displayed in Figure 7 based on UC3M's hyperspectral imaging method. The retrieved concentration values are good and very close to the expected ones for a gas cell which effective length is 43 cm.

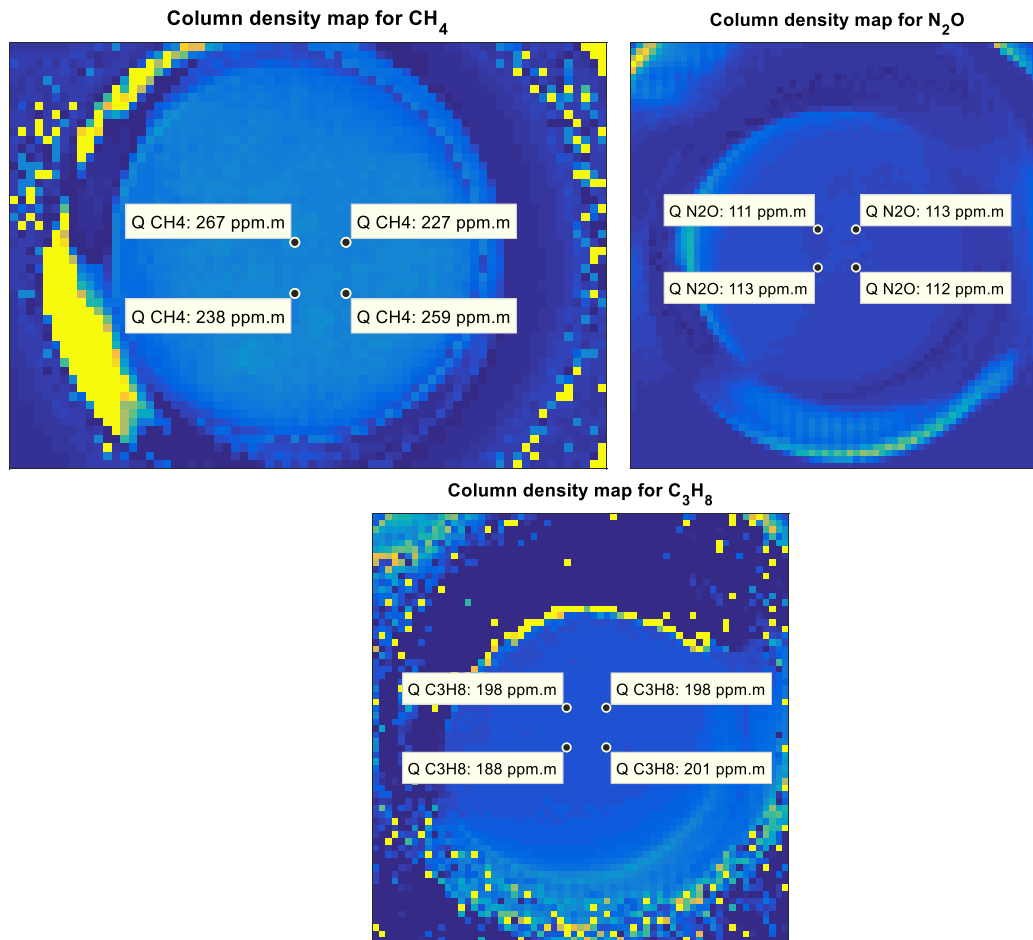


Figure 7. Column density maps obtained by UC3M for the three air pollutants prepared by CEM

In order to compare the accuracy of the obtained results, the Table 4 is presented where the column density (Q) central values (from an average of a 7x7 pixels square area which corners are illustrated in Figure 7) are compared with the expected values as CEM basis to prepare the gas mixtures. The retrieved concentration error is the standard deviation of the column density inside the mentioned 7x7 pixels square area.

Pollutant gas	Retrieved Q (7x7 area) (ppm·m)	Expected Q (ppm·m)	ϵ retrieved Q (%)
Methane (CH ₄)	250 ± 9.8	258	-3.1
Nitrous oxide (N ₂ O)	112.3 ± 1.4	107.5	+4.5
Propane (C ₃ H ₈)	199.7 ± 3.8	215	-7.1

Table 4. Retrieved concentration values from the prepared gas mixtures by CEM

From the previous information it can be concluded that the Q values for both nitrous oxide (N₂O) and methane (CH₄) can be retrieved with high accuracy by our method; whilst for propane (C₃H₈) the error is less than 10%. Furthermore, the standard deviation values could be obtained due to the selected central 7x7 pixels' area which gives a better perspective of the whole result to obtain concentration by this method, highlighting its advantage to get image information at a time (i.e. more than one point) of the gas cell.



3 OPO development and HCl measurements at VSL

Introduction

Nearly 40 years ago, hyperspectral imaging methods were first introduced in satellite and airborne imaging and it is now making its way into other fields such as mineralogy, plant science and laboratory practice [Chio 1985, Boubanga-Tombet et al., 2018]. Hyperspectral imaging has been shown to be a very powerful technique to characterize and analyze a wide range of samples. In order to make such quantitative studies, accurate radiometric and spectral calibrations of hyperspectral imaging data are necessary. A first step towards better calibration in order to obtain more robust images for multivariate analysis was made by Geladi and co-workers [Geladi et al., 2004]. Depending on the hyperspectral imager, different requirements are set for temporal, spatial and spectral features of the light source used for calibration of testing. The Fourier transform spectrometer (FTS) imaging system developed by U3CM within the framework of the IMPRESS II project has been applied to study the methane ν_1 symmetric stretch band of CH_4 centred at 2917 cm^{-1} (3428 nm). Within the same project VSL has worked on the development of infrared source for the testing and calibration of hyperspectral imagers in the fingerprint wavelength region which also covers the methane ν_1 band. The infrared source is based on a narrow line width continuous wave optical parametric oscillator (OPO). By rapidly tuning the OPO the spectral imager effectively sees a broadband source.

Materials and methods

The OPO is pumped by a 10 W fiber laser operating at 1064 nm which can be tuned mode hop free. The OPO cavity is used in a bow-tie configuration; all mirrors of the cavity are highly reflective for the signal wavelength (1.45-1.65 μm) and anti-reflection coated for both the pump wavelength and the idler wavelength. Within the cavity a periodically poled lithium niobite (PPLN) crystal is contained in an oven controlled to a temperature better than 0.1 $^\circ\text{C}$.

The OPO can be rapidly (10's of Hertz) tuned via 2 different mechanisms:

- 1) Tuning of the seed laser using a piezo attached to the fiber laser. At frequencies up to 10 Hz nearly the full modulation depth can be obtained (>15 pm). At higher frequencies there is some roll off but at 1 kHz it is still about 50% of the maximum tuning range. Seed laser tuning results in tuning of the idler wavelength up to 3 nm.
- 2) Inside the cavity an etalon is mounted on a galvo. Depending on the thickness of the etalon (here a 50 μm thick silicon etalon and a 400 μm thick uncoated YAG etalon were used) and on the parametric bandwidth of the PPLN crystal tuning over several nanometer (about 7-13 nm). Using thinner etalons or etalons made of a material with a higher refractive index enables wider tuning.

Wider tuning of the OPO is realized via either tuning of the crystal temperature or the poling period of the PPLN crystal. A total tuning range over more than 1 μm can be obtained. The output of the OPO is optimized for maximum idler output; the idler output power can be more than 2 Watt at some wavelengths. If required, also the output at the signal wavelength can be used but here the output power is limited to tens of milliwatt (replacing one of the high reflectivity cavity mirrors with an outcoupler can boost this power).

The output of an OPO is typically a gaussian beam with an exciting beam diameter of about 2 mm. For some applications the OPO beam intensity of hundreds of milli Watts will be too high leading

potentially to damage of the imager. Further, such a small beam diameter would only allow the simultaneous exposure of a limited number of pixels. Both shortcomings can be overcome by expanding the OPO beam using suitable optics such as diffusers which create a diffuse intensity pattern with a certain angular distribution. Reflective diffusers do not suffer from absorption losses as transmissive diffusers and can achieve very high average reflectance in the infrared. Engineered diffusers can offer customized patterns. Further, beam expanders (for the infrared region covering reflective beam expanders are typically preferred over diffractive beam expanders to avoid fringing or limited bandwidth)

Results

As a test gas hydrogen chloride (HCl) was used. Two small identical quartz cells (7 mm in length) were used, one filled with nitrogen and the other filled with a high amount fraction of HCl. Figure 1 shows a measurement of both cells using a FTIR spectrometer (Bruker Vertex 70v). The inset shows the derived absorbance. The line shown in grey (H^{35}Cl R(3) line centred at 2963.29 cm^{-1} according to HITRAN database) was used in the experiments using the OPO.

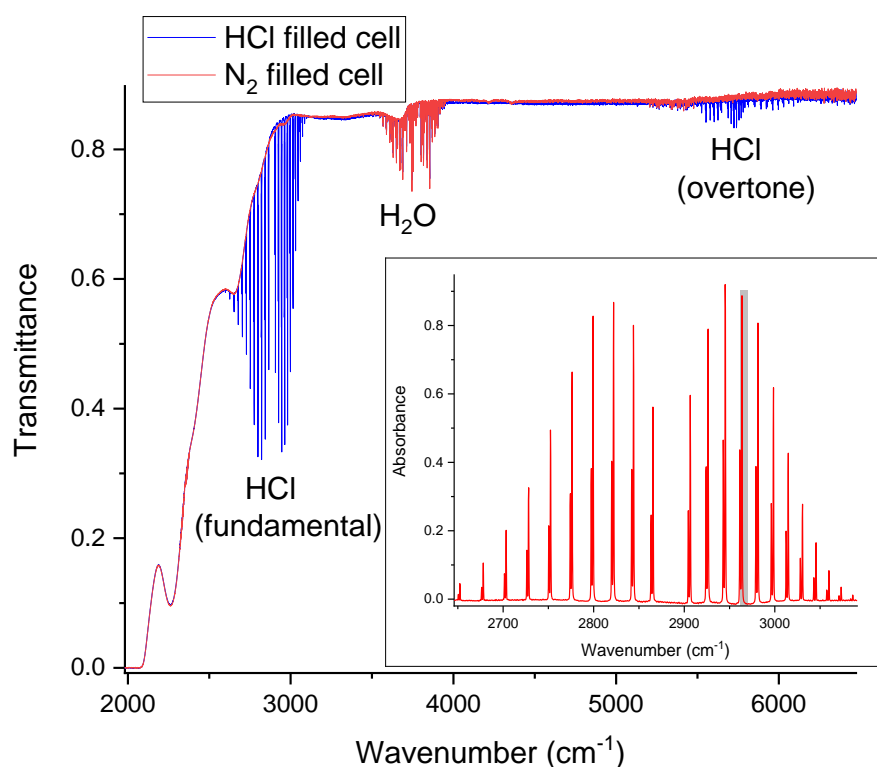


Figure 1 Measurement by FTIR spectrometer of the transmission of two identical cells, one containing HCl and the other N_2 . The inset shows the derived absorbance spectrum. The line at 2963 cm^{-1} (shown in grey) was used for the OPO experiments.

Figure 2 shows a measurement of HCl by scanning the OPO at a rate of 20 Hz. Also shown is a trace recorded using a 15 GHz etalon. In the OPO experiment strong fringes were observed as the cells are not anti-reflection coated and these were removed by the software.

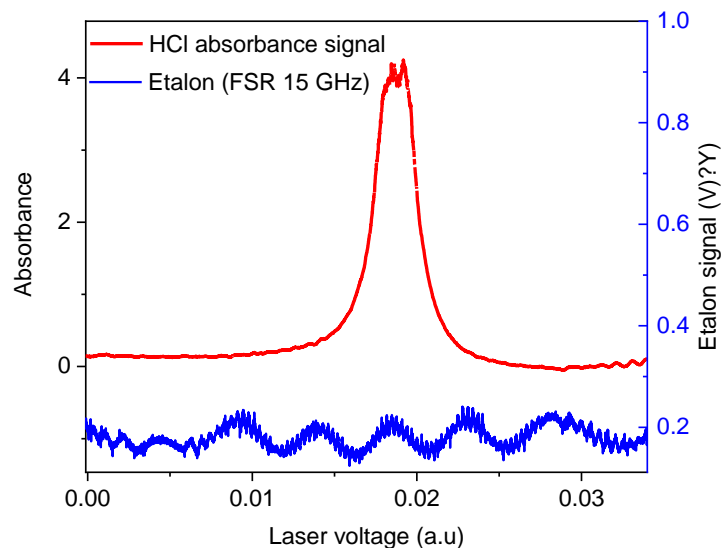


Figure 2 Direct absorption measurement of the HCl line centred at 2963.29 cm^{-1} . The OPO was tuned at a rate of 20 Hz over the absorption line.

To achieve wider tuning a thin etalon (50 μm thick) mounted on a galvo was used. Figure 3 shows the measurement results for the OPO operating in the $2.3 \mu\text{m}$ range. In this case the etalon was tuned slowly so that the wavelength meter could follow the tuning of the OPO. A tuning range of 13 nm is obtained in this case.

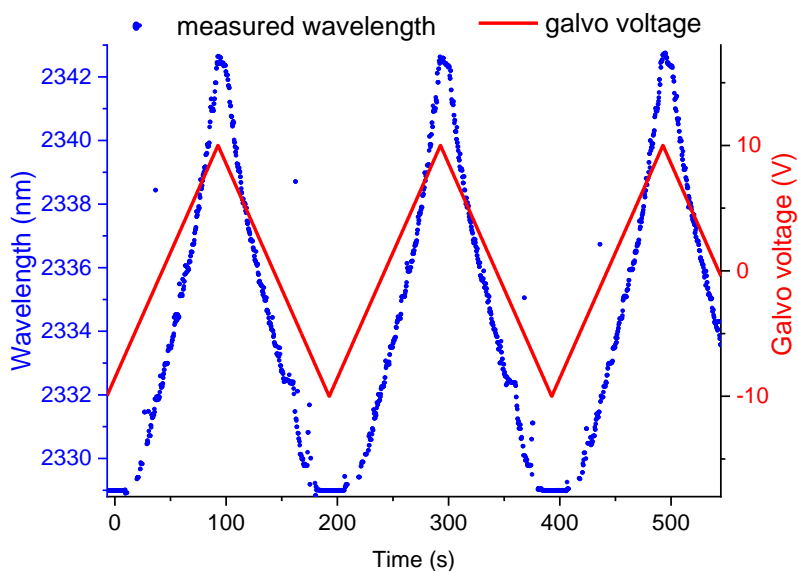


Figure 3 Tuning of the OPO using only etalon tuning.

While the current OPO has a limited continuous scanning range, it can be readily extended via various ways. The most promising methods are:



- 1) Using a pump laser with a wider continuous tuning. Klein and co-workers achieved tuning of the OPO idler wavelength from 3160 to 3500 by tuning of the fiber-laser wavelength over 33 nm through an intracavity acousto-optic tunable filter [Klein et al., 2003].
- 2) Electro-optic spectral tuning in which a high voltage is applied to a PPLN crystal with a special structure [O'Brien et al., 1999]. Recently, it was demonstrated output signal wavelength could be tuned from 1.373 to 1.749 μm with a corresponding idler tuning range from 2.863 to 1.972 μm by only changing the electric field applied to the crystal [Kumar et al., 2020].

Acknowledgements

The study was funded by The Joint Research Project 'Metrology for Air Pollutant Emission' (IMPRESS II) which is supported by the European Metrology Programme for Innovation and Research (EMPIR). The EMPIR initiative is co-funded by the European Union's Horizon 2020 research and innovation programme and the EMPIR Participating States.

References

1. Boubanga-Tombet, S., Huot, A., Vitins, I., Heuberger, S., Veuve, C., Eisele, A., ... & Chamberland, M. (2018). Thermal infrared hyperspectral imaging for mineralogy mapping of a mine face. *Remote sensing*, 10(10), 1518.
2. Chiou, W. C. (1985). NASA image-based geological expert system development project for hyperspectral image analysis. *Applied optics*, 24(14), 2085-2091.
3. Geladi, P., Burger, J., & Lestander, T. (2004). Hyperspectral imaging: calibration problems and solutions. *Chemometrics and intelligent laboratory systems*, 72(2), 209-217.
4. Klein, M. E., Gross, P., Boller, K. J., Auerbach, M., Wessels, P., & Fallnich, C. (2003). Rapidly tunable continuous-wave optical parametric oscillator pumped by a fiber laser. *Optics letters*, 28(11), 920-922.
5. O'Brien, N., Missey, M., Powers, P., Dominic, V., & Schepler, K. L. (1999). Electro-optic spectral tuning in a continuous-wave, asymmetric-duty-cycle, periodically poled LiNbO₃ optical parametric oscillator. *Optics letters*, 24(23), 1750-1752.
6. Kumar, C. S. P., Kim, B. J., Kim, D. W., Cha, M., Bae, I. H., Hong, K. S., & Lee, D. H. (2020, March). Ultra-broadband spontaneous parametric downconversion in periodically poled lithium niobate and electro-optic tuning of the optical parametric oscillation. In *Nonlinear Frequency Generation and Conversion: Materials and Devices XIX* (Vol. 11264, p. 112640E). International Society for Optics and Photonics.